

Excited-State Dynamics of Carotenoids in Light-Harvesting Complexes. 2. Dissecting Pulse Structures from Optimal Control Experiments

Emmanouil Papagiannakis,[†] Mikas Vengris,^{†,‡} Leonas Valkunas,^{‡,§} Richard J. Cogdell,^{||} Rienk van Grondelle,[†] and Delmar S. Larsen^{*,⊥}

Faculty of Sciences, Vrije Universiteit Amsterdam, De Boelelaan 1081, 1081 HV Amsterdam, The Netherlands, Faculty of Physics, Vilnius University, Saulėtekio Avenue 9, Block 3, 10222 Vilnius, Lithuania, Institute of Physics, Savanoriu Avenue 231, 02300 Vilnius, Lithuania, Institute of Biomedical & Life Sciences, University of Glasgow, Glasgow, United Kingdom, and Department of Chemistry University of California, Davis, One Shields Avenue, Davis, California 95616

Received: August 17, 2005; In Final Form: November 15, 2005

Dispersed multipump–probe (PPP) spectroscopy was used to explore the role of saturation, annihilation, and structured pulses in recent coherent control experiments on the light-harvesting 2 complex from *Rhodospseudomonas acidophila* (Herek et al. *Nature* **2002**, 417, 533). We discuss the complimentary aspects between the PPP technique and coherent control studies, in particular the ability to dissect complicated pulse structures and the utility in exploring incoherent mechanisms. With the aid of a simple multistate model involving only population dynamics, we illustrate how the optimized structured pulses may be explained in terms of an interplay between excited-state populations, saturation, and annihilation. Furthermore, we discuss the experimental conditions that are required for incoherent effects to contribute to control experimental signals, with particular emphasis on pulse intensities, and show that the optimization of a ratio of conservative signals (i.e., not modulated by external dynamics) is required to exclude saturation effects from coherent control studies.

1. Introduction

In the past decade, it has been shown that specially designed laser pulses can be used to coerce photoinduced reactions into specific optimized outcomes^{1–5} including amplified population excitation,^{6,7} enhanced branching ratios in dissociating systems,^{8,9} and selective excitation of vibrational modes.¹⁰ These outcomes result from the optimization of the excitation pulse characteristics (e.g., phase, amplitude, timing, and polarization), frequently combined with the use of iterative learning algorithms based on optimal control theory^{11–14} and pulse shaping.^{6,15–17} Often such control studies entail the simultaneous measurement of multiple signals from the sample after excitation (e.g., detached electron intensities, molecular fragments, or spectroscopic features), and in many such experiments, the data can be interpreted within the context of transient absorption, or pump–probe (PP), experimental results. Frequently the obtained optimized pulse for enhancing a specific reaction result is a structured pulse sequence with specific separations between constituent subpulses.^{8,18,19} The dissection of these optimized structured pulses into contributions from individual subpulses is essential in understanding how the applied complex electric fields manipulate the system under study.

Recently, Herek et al.¹⁸ demonstrated how coherent control techniques can be extended to complex, multichromophore, biological systems. These authors used optimized laser pulses

to optically excite the $S_0 \rightarrow S_2$ transition of the rhodopin glucoside carotenoid within the light-harvesting 2 (LH2) protein complex from the purple photosynthetic bacterium *Rhodospseudomonas (Rps.) acidophila*. The authors observed a change of the efficiency of excitation energy flow proceeding along the internal conversion (IC) pathway (from S_2 to S_1) versus the excitation energy transfer (EET) from S_2 to the B850 bacteriochlorophyll (BChl) molecules^{20–22} and found that the optimal IC/EET ratio resulted from the generation of a structured pulse sequence with 8–10 ~30-fs transform-limited subpulses separated by ~250 fs.^{18,23} Moreover, a unique optical phase-shifting relationship between each subpulse was identified that also modulated the IC/EET efficiency, which was supportive of their claim that an underlying coherent mechanism is responsible for the observed pulse separations.

This paper is the second in a series that explores the photoinduced dynamics of carotenoids in (LH) protein complexes. In the first paper of the series (hereby referred to as paper 1),²⁴ we observed that the population ratio of S_1 and S^* of rhodopin glucoside in the LH2 complex of *Rps. acidophila* is dependent on the excitation intensity. To simultaneously explain both the time-resolved and intensity-dependent PP measurements, we proposed modifying the previously proposed kinetic models to either introduce (1) multiple ground-state populations with each exhibiting different relaxation dynamics or (2) an extra light-induced transition, which upon excitation promotes the population to a higher excited state. Both models describe the intensity dependence observed in the measured PP signals and reproduce the same underlying dynamical time scales. In this paper, the second of the series, we modified the PP experimental setup to mimic the incoherent aspects of the optimal control experiment of Herek et al.¹⁸ and used two

* Author to whom correspondence should be addressed. E-mail: dlarsen@chem.ucdavis.edu.

[†] Vrije Universiteit Amsterdam.

[‡] Vilnius University.

[§] Institute of Physics.

^{||} University of Glasgow.

[⊥] University of California, Davis.

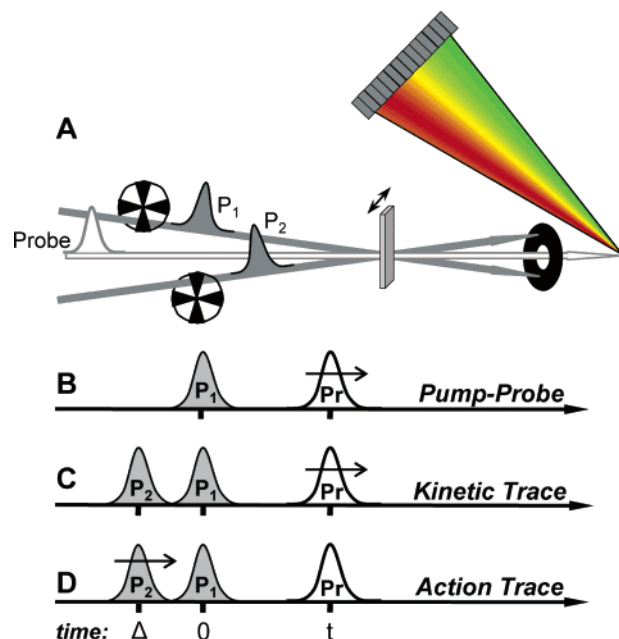


Figure 1. (A) Multipump dispersed PP experimental setup and (B) different pulse timing schemes.

independently timed laser pulses to excite rhodopin glucoside in the LH2 complex of *Rps. acidophila* (Figure 1). After excitation by either (or both) pump pulses (P_1 and P_2), a third broad-band probe pulse interrogates the sample, as in standard dispersed PP experiments. The simultaneous and independent measurements of the respective dynamics induced by each (and the combination of both) excitation pulse(s) allows the direct characterization of the multiphoton interactions often proposed to explain optimal control results.

Proper interpretation of the results from optimal control studies requires that certain questions be addressed, including:

- What are the relevant characteristics (e.g., kinetics and amplitudes) of the signals involved?
- What phenomena contribute to an observed optimized separation and hence multipulse structures in control experiments?
- How do incoherent mechanisms, like saturation and annihilation, affect multiphoton excitation dynamics?
- What excitation pulse intensities are required to minimize interfering effects?

These questions will be addressed below as we show how the combination of multipump measurements and numerical simulations using a kinetic model that incorporates the proper intensity dependence of the underlying mechanisms (e.g., saturation and annihilation) can help to dissect optimal control signals into contributions originating from incoherent dynamics observed in simple PP signals.

2. Experimental Section

2.1. Sample Preparation. The LH2 complexes were extracted from cultures of *Rps. acidophila* strain 10050 and isolated as detailed previously.²² The complexes were suspended in a Tris/HCl buffer (20 mM, pH 8) with 0.1% LDAO detergent to prevent significant aggregation and had an optical density of 0.25 mm⁻¹ at 525 nm. The 525-nm excitation laser pulses selectively excite rhodopin glucoside to its S_2 state; the sample was kept in a rapidly shaking 1-mm quartz cuvette to avoid exposure to multiple pulses; no sign of sample degradation was observed in the absorption spectra collected before and after experiment.

2.2. Experimental Setup and Signals. The experimental setup described in paper 1 was used with several modifications, with the major change requiring the splitting of the 525-nm excitation pulses generated by a home-built, noncollinear optical parametric amplifier (NOPA) into two separate optical delay paths, each equipped with a computer-controlled mechanical delay line to provide independent timing. Both pump beams were focused in the sample (spot size $\sim 300 \mu\text{m}$) with separate 10-cm focal length quartz lenses, and the probe light was focused (spot size $\sim 50 \mu\text{m}$) with off-axis (90°) parabolic mirrors. All three beams propagated in the same plane with a $\sim 2^\circ$ angle between them, and separate phase-locked choppers were used to modulate the two pump beams (at 500 and 250 Hz) independently. The time duration and bandwidths of the excitation pulses were ~ 40 fs and $\sim 550 \text{ cm}^{-1}$, respectively. The polarization of the two pump beams were parallel and set to magic angle (54.7°) with regard to that of the white light probe. A rapidly rotating thin glass disk (< 1 mm) was inserted into one of the pump beam lines to randomize the optical phase relationship between the two excitation beams and exclude any coherent effects from the measured signals.

This setup allows the simultaneous collection of multiple signals, which can be manipulated to emphasize different aspects of the multipump dynamics.^{25,26} The multidimensionality of these signals can be exploited by measuring and presenting the data in different ways (Figure 1).^{26,27} The most direct and intuitive way to collect such three-dimensional data is in the form of a “kinetic trace” (Figure 1C), where the first and second excitation pulses are set at fixed times and the signals are collected by measuring the change in the transmission of a delayed probe pulse delay, as in PP experiments. However, the connectivity between transient states is often more clearly observed in an “action trace” (Figure 1D), which is collected by delaying the second pump pulse with the first pump and probe pulses kept fixed. When the delay of the second pump pulse is scanned (with a fixed probe time), the temporal efficiency of influencing a specific long-time PP spectrum is observed. While kinetic traces directly monitor the dynamics of the multipump process, action traces measure the asymptotic effects on a PP spectrum at a specified probe time. Because of this, the action trace timing scheme is used to mimic coherent control experiments where the terminal, or long-time, properties of the system are measured as the excitation pulse properties are experimentally varied.

Since both pump pulses are resonant with the ground-state population(s), each will generate an independent PP signal, pump₁–probe (P_1P) and pump₂–probe (P_2P), for the fixed pump (P_1) and moving pump (P_2) pulse, respectively. If the pump pulses excite the sample with a specified temporal separation, Δ , then the resulting collected signal is then termed the pump₁–pump₂–probe (PPP) signal. It is often useful to explore the P_2 -induced changes to the P_1P signals, resulting in double-difference signals that highlight the multipump-induced effects in the PPP experiment

$$\Delta\Delta\text{OD}(\lambda, t, \Delta) = \text{PPP} - P_1P - P_2P \quad (1)$$

where t is the probe time and Δ is the delay of the second pump pulse, both with respect to the fixed P_1 pump pulse (at $t = 0$). A nonzero $\Delta\Delta\text{OD}$ signal suggests that the corresponding PP signals influence each other and that the PPP signal *cannot* be described simply as the sum of the two corresponding PP signals. Since the time dependence of the $\Delta\Delta\text{OD}$ signal includes both P_1P and P_2P dynamics, a relative $\Delta\Delta\text{OD}$ signal can be

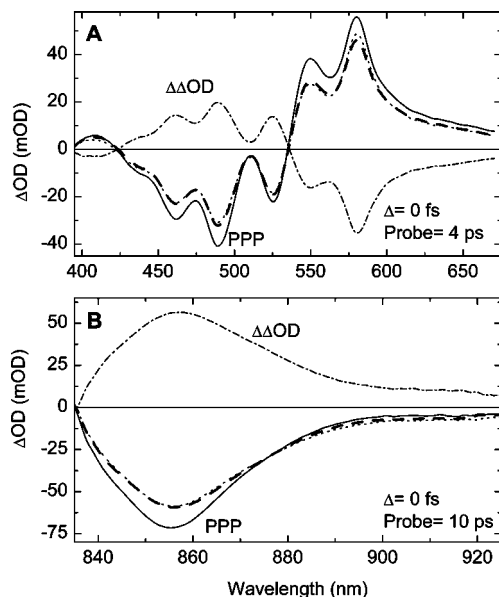


Figure 2. Measured multipulse spectra with $\Delta = 0$ fs. (A) Visible spectral probe window probed at 4 ps and (B) NIR spectral window probed at 10 ps. For both panels: P₁P (thick dashed curves), P₂P (dotted curves), PPP (solid curves), and $\Delta\Delta\text{OD}$ (dash-dot curves). The excitation intensity was ~ 60 nJ per pulse.

constructed to highlight the amplitude and dynamics induced by multipumping the sample

$$\Delta\Delta\text{OD}_{\text{rel}}(\lambda, t, \Delta) = \frac{\Delta\Delta\text{OD}(\lambda, t, \Delta)}{P_1P + P_2P} \quad (2)$$

It must be noted that the multipump experiments presented here are sensitive only to “incoherent” effects and cannot directly investigate coherent properties. Consequently, the complex phase dependence also observed in the Herek et al. study^{18,23} is not addressable within the limits of our experimental and simulation studies.

3. Experimental Results

3.1. Kinetic Trace Signals. The multipump signals collected after exciting rhodopin glucoside in LH2 with 525-nm laser pulses and probing across the visible and near-infrared (NIR) regions are contrasted in Figure 2. These spectra were measured with a zero temporal separation between the two pump pulses ($\Delta = 0$) and at probe delays of 4 ps for the visible and 10 ps for the NIR signals. At first glance, the PPP spectrum in the visible region (solid line) is nearly identical to the P₁P and P₂P spectra, although with a larger amplitude since it corresponds to twice the excitation energy (i.e., from both excitation pulses). This is also the case for the NIR signals in Figure 2B. Upon closer inspection though, if the visible PPP and PP spectra are normalized, then a clear difference in the relative amplitudes of the S₁ and S* bands at 580 and 550 nm, respectively, is observed (not shown). This subtle, but important, property is discussed in detail in part 1.

For both the visible and the NIR spectral windows, the amplitude of the PPP signal is not equal to the sum of the two separate PP signals (thick dashed and dotted lines), and nonzero $\Delta\Delta\text{OD}$ signals can be constructed (dash-dot lines). The marked similarity of the $\Delta\Delta\text{OD}$ to the corresponding PP signals shows that the observed depletion (i.e., the $\Delta\Delta\text{OD}$ signal) affects the ground-state bleach (GSB) and excited-state absorption (ESA) regions alike. This is in contrast to other dispersed multipulse

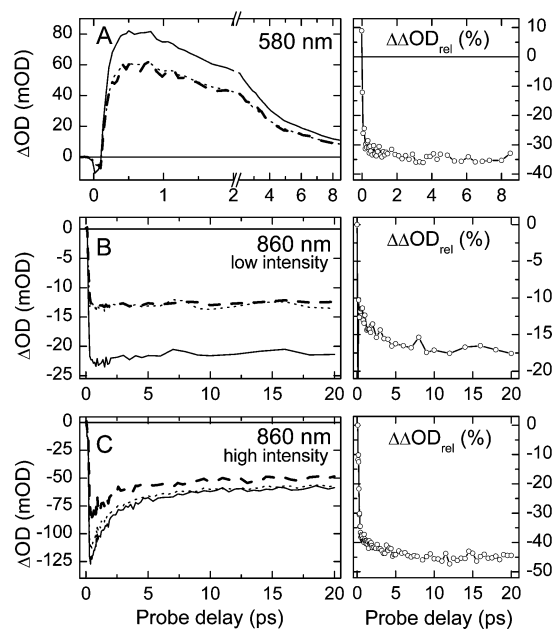


Figure 3. Kinetic traces measured at 580 and 860 nm. The left panels show the raw signals, while the right panels show the corresponding $\Delta\Delta\text{OD}_{\text{rel}}$ signals (eq 2): P₁P (filled circles), P₂P (open circles), PPP (filled squares), and $\Delta\Delta\text{OD}_{\text{rel}}$ (open circles). Note the break in the time axis at 2 ps for the raw signals at 580 nm. The high- and low-intensity measurements were performed with ~ 60 and ~ 15 nJ per pulse, respectively, and the visible data were collected at high intensity.

experiments.^{26,28,29} While the visible signals are mostly sensitive to the excited states of rhodopin glucoside, the NIR signals are sensitive to the B850 population,³⁰ which exhibits a strong negative signal composed of GSB and stimulated emission (SE) contributions.³¹

Because the PPP and PP spectra strongly resemble each other, the multipump signals are best explored in the time domain. Figure 3 contrasts the kinetic trace signals (with $\Delta = 0$) at selected probe wavelengths. Both the P₁P and P₂P signals (thick dashed and dotted lines) exhibit dynamics similar to those previously measured for the S₁ population dynamics.^{20,21,24} The 580-nm signal (Figure 3A) exhibits SE from the initially excited S₂ state (early negative signals) and is dominated by ESA from the S₁ population, whereas a multipump depletion (i.e., a nonzero $\Delta\Delta\text{OD}$ signal) exists at all probe times. Since the PPP, P₁P, and P₂P signals exhibit nearly identical dynamics, the observed depletion can be determined from the corresponding $\Delta\Delta\text{OD}_{\text{rel}}$ visible signal (Figure 3A, right panel). This depletion is generated nearly instantaneously and maintains a constant value of $\sim 33\%$ of the sum of the P₁P and P₂P signals for the duration of the experiment.

In contrast, the NIR signals exhibit a similar depletion that is not constant but increases on multiple time scales. Consequently, the PPP signals *must* exhibit dynamics different from the two PP signals, which is observed in the corresponding $\Delta\Delta\text{OD}_{\text{rel}}$ signals (Figures 3B and 3C, right panels). In these signals, an instrument-limited rise in the depletion is observed followed by a weaker amplitude 2-ps component. Comparing the NIR $\Delta\Delta\text{OD}_{\text{rel}}$ signals measured at both high and low excitation intensities shows that although the multipump depletion is observed in both intensity regimes, the amplitude of the initial rise differs greatly. While the high-intensity signals exhibit a $\sim 35\%$ instrument-limited depletion (which is also shared by the visible data measured at the same pulse intensities), the amplitude of the initial rise of the low-intensity signals is

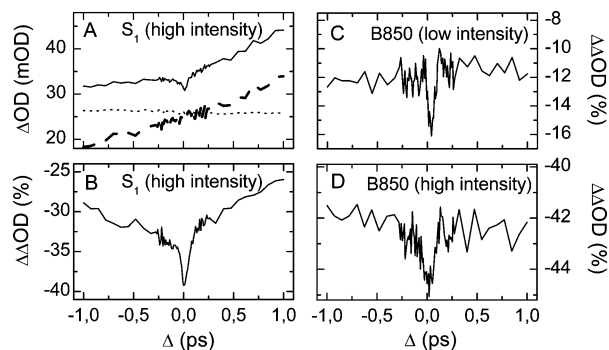


Figure 4. Action trace data. (A) The S_1 population measured at 580 nm and probed at 4 ps. Lines have the same designations as in Figure 2. (B) The reconstructed $\Delta\Delta OD_{rel}$ signals for the raw data in part A and (C and D) the corresponding $\Delta\Delta OD_{rel}$ signals for the B850 population probed at 10 ps and at 860 nm and at different pulse intensities. The high- and low-intensity measurements were performed with ~ 60 and ~ 15 nJ per pulse, respectively.

distinctly smaller ($\sim 12\%$), although the slower component appears with a similar amplitude to the higher-intensity signals. Kinetic trace signals with nonzero Δ values exhibit similar kinetics (not shown) with small, albeit key, differences that are more easily observed in the action trace signals.

3.2. Action Trace Signals. The action trace signals for the S_1 (580 nm) and B850 (850 nm) populations, probed at 4 and 10 ps, respectively, are compared in Figure 4 with different excitation pulse intensities. The 580- and 850-nm signals at these probe times are selectively sensitive to the S_1 and B850 populations, respectively. The raw P_1P and P_2P action trace signals for S_1 exhibit different trends with respect to Δ , depending on whether the stationary P_1 (dots) or P_2 (dashed line) pump pulse is used to initiate the dynamics (Figure 4A). This is expected; the ~ 3 -ps relaxation dynamics of the S_1 population can be clearly observed in the 4 ± 1 -ps probe window for the action trace. Three important features can be identified in the S_1 action trace signals: (1) The PPP signal (solid line) has a decay component that is directly correlated with the S_1 lifetime as the P_2 pump pulse shifts away from the probe pulse. (2) The corresponding $\Delta\Delta OD_{rel}$ signal (Figure 4B) shows that the multipulse depletion observed in the kinetic traces (Figure 3) exists at all pulse separations but is strongest at $\Delta = 0$. As discussed in the following section, the peak in the depletion can be directly attributed to saturation, and the offset to the partial depletion of ground state (i.e., reducing the available ground-state population) after excitation by the first pump pulse.

The NIR action trace signals (B850 population) exhibit similar, albeit distinctly different, properties. The $\Delta\Delta OD_{rel}$ signal for the high-intensity measurements of the B850 population (Figure 4D) shows a clear depletion at $\Delta = 0$, although with a significantly smaller amplitude ($\sim 2\%$ or 5% of the offset) than those observed for the S_1 signals in Figure 4B ($\sim 8\%$ or 24% of the offset). In contrast, the amplitude of the depletion in the low-intensity $\Delta\Delta OD_{rel}$ signal (Figure 4C) is noticeably larger on an absolute ($\sim 5\%$) and relative (45% of the offset) scale. It is clear that increased excitation intensities lead to reduced depletion and hence weaker dependencies of the multipump signals on the pulse separation, Δ . As discussed below, this effect is ascribed to singlet–singlet annihilation.

4. Numerical Calculations

The multistate kinetic models presented in paper 1 to explain the measured time-resolved and intensity-dependent PP signals of LH2 of *Rps. acidophila* require the introduction of either a

ground-state inhomogeneity or an additional photoinduced transition in the excited-state manifold of the carotenoids.²⁴ In the following sections, only the two-photon model is used for the numerical simulations used to interpret the multipump experimental results, although nearly identical results can be obtained from the inhomogeneous model. The two-photon model in paper 1 was constructed to account for the behavior of the carotenoid signals without considering secondary intensity-dependent effects such as singlet–singlet annihilation among bacteriochlorophylls. Below, this model will be extended to incorporate an appropriate description of the annihilation dynamics with the corresponding excitation intensity dependences.

The excited B850 population (after 525-nm excitation of LH2) is produced via EET from the carotenoids and decays via three nonradiative pathways: (1) IC to the ground state, (2) intersystem crossing to generate BChl triplets that are in turn quenched by the carotenoids, or (3) singlet–singlet annihilation. The first two channels are observed on a nanosecond time scale, while annihilation occurs on a significantly faster time scale (~ 5 ps) and is comparable with the S_1 population decay (Figure 3).³² While IC and intersystem crossing pathways originate from the decay kinetics of single excitations, annihilation results from multiple-excitation interactions³³ and is manifested as a “disappearance” of excitations as the system evolves in time. As a result, the simple first-order differential equations that are often used to describe population flow fail to capture annihilation effects properly; however, as discussed below, with the suitable approach, annihilation dynamics can be addressed and implemented in the multistate model.³³

In paper 1, we modeled the population flow into the BChl manifold as unidirectional and with no population decay. In these models, $d[B850]/dt$ represents the flow of excited-state population into the B850 manifold from rhodopin glucoside. To properly simulate annihilation dynamics, we model the B850 population not with respect to the total B850 concentration but in terms of the population of LH2 rings with a specified number of excited B850 molecules.³⁴ Thus the population of the zero-excited, singly excited, doubly excited, etc. rings ($[B850]_i$ with $i = 0, 1, \dots, 9$) can be independently modeled; such an approach ensures the proper statistics of B850 excitations based on the amplitude of excitations flowing via EET pathways from the carotenoid. The following set of coupled differential equations for the B850 manifold dynamics can then be constructed

$$\frac{d[B850]_0}{dt} = -\frac{d[B850]}{dt}p_0 + k_{B850}^{1 \rightarrow 0}[B850]_1 \quad (3a)$$

$$\frac{d[B850]_i}{dt} = \frac{d[B850]}{dt}p_{i-1} - \frac{d[B850]}{dt}p_i - k_{B850}^{i \rightarrow i-1}[B850]_i + k_{B850}^{i+1 \rightarrow i}[B850]_{i+1} \quad (3b)$$

($i = 1, 2, \dots, 8$)

$$\frac{d[B850]_9}{dt} = \frac{d[B850]}{dt}p_8 - k_{B850}^{9 \rightarrow 8}[B850]_9 \quad (3c)$$

where the probability of promoting a B850 ring with i excitation(s) to $(i + 1)$ excitation(s) is proportional to its relative occupation

$$p_i = \frac{[B850]_i}{\sum_{i=0}^9 [B850]_i} \quad (4)$$

TABLE 1: Annihilation Parameters^a

decay constants	$k_{\text{B850}}^{1 \rightarrow 0}$	$k_{\text{B850}}^{2 \rightarrow 1}$	$k_{\text{B850}}^{3 \rightarrow 2}$	$k_{\text{B850}}^{4 \rightarrow 3}$	$k_{\text{B850}}^{5 \rightarrow 4}$	$k_{\text{B850}}^{6 \rightarrow 5}$	$k_{\text{B850}}^{7 \rightarrow 6}$	$k_{\text{B850}}^{8 \rightarrow 7}$	
$k_{\text{B850}}^{9 \rightarrow 8}$	750 ps ⁻¹	1.5 ps ⁻¹	800 fs ⁻¹	150 fs ⁻¹	30 fs ⁻¹	10 fs ⁻¹	10 fs ⁻¹	10 fs ⁻¹	10 fs ⁻¹

^a The error bars for $k_{\text{B850}}^{2 \rightarrow 1}$ are $\sim 10\%$, while for $k_{\text{B850}}^{3 \rightarrow 2}$ and higher constants they are limited to $\sim 20\%$.

To properly combine this annihilation model with the multistate models in paper 1, we scale the initial population of LH2 rings, $[\text{B850}]_0$, to the number of carotenoids in the LH2 ring (9). The number of excitations introduced into the B850 manifold is directly controlled by the interplay between intensity of the excitation pulse(s) and the rhodopin glucoside carotenoid manifold. The total excited B850 population, which is directly observed in NIR PP measurements, is then

$$[\text{B850}]_{\text{tot}} = \sum_i i[\text{B850}]_i \quad (5)$$

As excitations flow into the B850 manifold, progressively higher $[\text{B850}]_i$ states become occupied, which subsequently decay via annihilation. The decay of the B850 population from the annihilation of i excitations to $(i - 1)$ excitation(s) is single-exponential, and we presume that the annihilation from the doubly excited state is the predominant process describing the slowest annihilation decay and the relaxation from more-than-doubly excited state induces faster annihilation kinetics (Table 1). These parameters were determined from a direct comparison of the simulated $[\text{B850}]_{\text{tot}}$ from the model to the time-resolved 860-nm data (Figure S3). Within this model, the annihilation-free response, $[\text{B850}]_{\text{AF}}$, can be easily simulated by setting the annihilation time constants, $k_{\text{B850}}^{i \rightarrow i-1}$, to zero. This is particularly useful, as a comparison of simulations with and without annihilation is insightful to identify annihilation effects. It should be noted that both the intensity threshold and the time scales of annihilation are fully incorporated in this model; i.e., the annihilation onset occurs at a 9 times lower intensity than the saturation. However, not included are intermediate EET acceptor populations such as the excited electronic states of the B800 BChl, the Q_x electronic state of B850, and potential contributions from B850 exciton dynamics.³⁵ Because this kinetic model describes only population dynamics and treats the matter–field interactions at the photon level (i.e., two interactions with the electric field per photon),³⁶ the resulting simulations can be interpreted exclusively in terms of population dynamics.

The population kinetics simulated from the two-photon model for all the observed states are compared in detail in paper 1; here we will focus exclusively on the S_1 and B850 states, which were the only explored populations in the Herek et al. LH2 study.¹⁸ The simulated PPP signals for these states measured with $\Delta = -500$ fs are contrasted in Figure 5A. Although both pump pulses affect the full temporal properties of these signals, their individual influences are best observed in the rise dynamics, where a stepwise increase of the signals is clearly identified. Moreover, both the S_1 and the B850 populations exhibit qualitatively similar decay dynamics although the B850 signal decays to a finite level ($\sim 12\%$) and the S_1 population decays completely to zero. Note that even though both populations decay on comparable time scales (with the pulse intensities used) the decay of the B850 population results from singlet–singlet annihilation, which is of fundamentally different origin than the IC mechanism responsible for the decay of S_1 . The intensity dependence of these two mechanisms underlies the interpretation extracted from the multiple-pump data in Figures 2–4. The intensity dependence observed for the S_1 population follows a typical saturation-like trend (although with a weak deviation

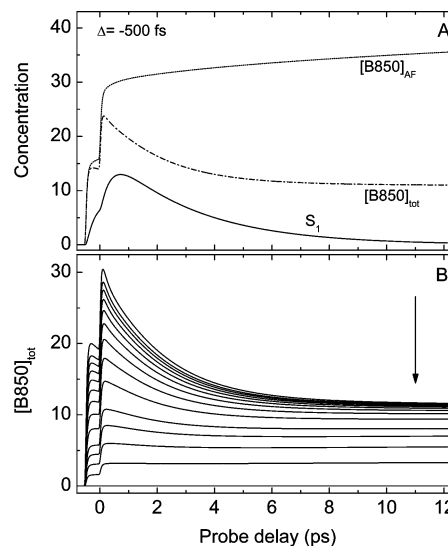


Figure 5. Simulated population kinetic curves with the two-photon model for LH2 modeled with a pump–pulse separation $\Delta = -500$ fs. (A) The S_1 population on the carotenoid and the B850 population. The $[\text{B850}]_{\text{tot}}$ signal with annihilation (dot–dashed line) is contrasted with the annihilation-free limit, $[\text{B850}]_{\text{AF}}$ (dotted line). (B) Simulated $[\text{B850}]_{\text{tot}}$ population with pulse intensities from 10 to 125 nJ. The arrow shows the trend toward decreased pulse intensities. The parameters used in all the model calculations are tabulated in Table 3 of paper 1 and Table 1 in this paper. The PPP signals were simulated with 35 fs (fwhm) pulses with ~ 60 nJ (6 au) intensity.

that is attributed to the additional transition in the two-photon model), but the annihilation dynamics in the B850 population exhibits a distinctly different intensity dependence, where as the pump intensity increases a faster-than-saturation loss of population becomes evident. This is illustrated in the simulated PPP signals for B850 generated with different excitation intensities (Figure 5B).

The simulated kinetic trace signals for the S_1 and B850 populations, generated with the same model parameters as in Figure 5, are overlaid with the corresponding simulated multipump signals in Figure 6. Because the pulse energies are equal for each pump pulse, both the P_1P (dotted lines) and the P_2P signals (thick dashed lines) exhibit identical amplitude and dynamics, albeit shifted by $\Delta = 0.5$ ps. The PPP signal (solid curve) exhibits a double step rise, with each step associated with a pump pulse; the ~ 3 -ps decay of the S_1 population attributed to its excited-state lifetime is observed, and the decay of the $[\text{B850}]_{\text{tot}}$ population is directly attributed to annihilation and is not observed in the $[\text{B850}]_{\text{AF}}$ signals. The $P_1P + P_2P$ signal (dot–dashed curve) is the predicted double-pump signal, assuming no interactions between the two PP signals. The $\Delta\text{AOD}_{\text{rel}}$ signal for S_1 (i.e., the relative difference between $P_1P + P_2P$ and PPP) is qualitatively similar to the experimental kinetic trace signals in Figure 3 and exhibits an instrument-response-limited rise with no further observable dynamics (Figure 6A, right panel). Within the context of the model, the dual-pump depletion is a direct consequence of saturation, where the number of absorbed photons is a nonlinear function of excitation pulse intensity. The $\Delta\text{AOD}_{\text{rel}}$ signals predicted for the annihilation-free B850 population ($[\text{B850}]_{\text{AF}}$) exhibit qualitatively similar dynamics with the S_1 population signals (Figure

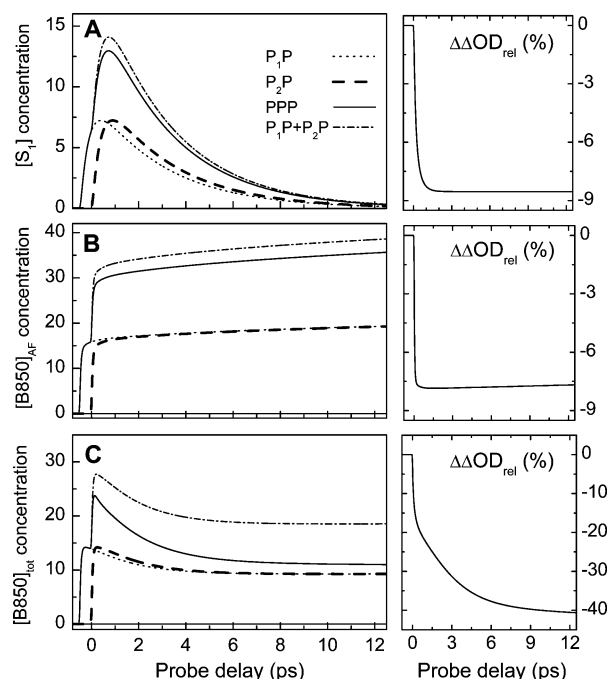


Figure 6. Simulated kinetic trace signals with $\Delta = -500$ fs. The (A) $[S_1]$, (B) annihilation-free $[B850]_{AF}$, and (C) full $[B850]_{tot}$ signals are contrasted. The $\Delta\Delta OD_{rel}$ curves (eq 2) for the corresponding concentration signals are shown in the panels to the right of the raw signals. The curves are labeled as marked in the legend of part A, and the simulations were performed with the model parameters outlined in the caption of Figure 5.

6B, right panel), because both populations are produced from the same excitation pulse and are simultaneously affected by the same saturation conditions. The small difference in final depletion level is attributed to different intensity-dependent EET pathways that funnel excitations into the B850 manifold from the carotenoid excited states.

The $[B850]_{tot}$ population dynamics (subject to annihilation) differs distinctly from the annihilation-free ($[B850]_{AF}$) signals. The depletion between the $P_2P + P_1P$ and PPP signals clearly increases in time (Figure 6C), which exhibits an instrument-response-limited rise with a slower, ~ 1.5 ps gain. As with the $[S_1]$ and $[B850]_{AF}$ populations, the rapid rise in the depletion results from saturation, but with a slower rise ascribed to singlet–singlet annihilation. A full quantitative interpretation of the annihilation model discussed above in strongly annihilating systems such as LH2 and other multichromophoric samples will be outlined elsewhere.³⁷ These depletion effects are best observed in the action trace signals, where the $[S_1]$ populations exhibit a pronounced dip at $\Delta = 0$ in both the PPP and the $\Delta\Delta OD_{rel}$ signals (Figure 7). The width of this depletion “dip” is determined by the temporal width (40 fs) and intensity (60 nJ) of the excitation pulses convolved over the lifetime of the S_2 state (~ 60 fs).²⁴ Hence, when the excited-state population has evolved away from S_2 , a saturation-induced depletion dip is not observed in the action signals. However, the depletion attributed to the loss of ground-state population (from the first excitation pulse) that is available for pumping by the second excitation pulse is observed as a near static nonzero $\Delta\Delta OD$ offset.

5. Discussion

5.1. Intensity Thresholds. The identification of the nature, number, and timing of the relevant matter–field interactions is important in interpreting the complex multipulse structures often

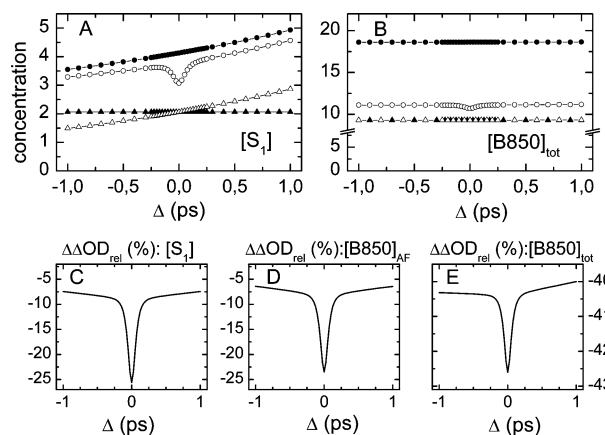


Figure 7. Simulated action traces for the S_1 and B850 populations probed at 4 and 10 ps, respectively. (A) S_1 population signals and (B) simulated $[B850]_{tot}$ signals are contrasted. The respective $\Delta\Delta OD_{rel}$ curves for the $[S_1]$, $[B850]_{AF}$, and $[B850]_{tot}$ signals in are shown in parts C–E, as labeled. The P_1P (filled triangles), P_2P (open triangles), and PPP (open circles) signals are shown with the predicted $P_1P + P_2P$ signal (filled circles). Note that the P_1P and P_2P signals for the $[B850]_{tot}$ signals overlap nearly completely in the plot. The simulations were performed with the model parameters outlined in the caption of Figure 5.

obtained from optimal control studies. The characterization of the excitation intensity thresholds at which different phenomena are observable is instrumental in pursuing this goal. The numerical simulations presented in section 4 describe the matter–field interactions only at the intensity level (i.e., via photon interactions) and cannot address coherent control mechanisms that have been formulated at the more fundamental electric-field magnitude level.^{2,4,38,39}

In experiments involving multiple interactions between the sample and the applied laser field (e.g., photon echoes, multipump, and optimal control studies among others), the measured signal is generated with an amplitude that is directly related to the transition dipole moment, μ , of the ground state of the sample. Because the LH2 samples typically used in time-resolved experiments are actually ensembles of subsystems (i.e., rings that contain multiple pigments), multiple interchromophore interactions may contribute to the experimental observations.³³ A simple, yet useful, relationship can be constructed to estimate the probability of initiating different light-induced processes involving n matter–field interactions and k chromophores (excluding exciton effects³³)

$$p_{k,n} \approx k | \langle e | \vec{E} \cdot \vec{\mu} | g \rangle |^n \quad (6)$$

This simple relationship assumes a constant $\vec{\mu}$ during the sequence of matter–field interactions between the ground, $|g\rangle$, and excited, $|e\rangle$, electronic states and since $\langle e | \vec{E} \cdot \vec{\mu} | g \rangle \ll 1$, increasingly larger electric-field amplitudes, $|E|$, are required to observe processes with a progressively higher number of interactions.³⁶ Hence, at sufficiently high excitation intensities, multiple mechanisms may contribute to signals with amplitudes that may be estimated according to eq 6. Here we identify three relevant intensity thresholds for generic optimal control experiments (and all optical signals in general) of multichromophoric systems: (1) optimal/coherent control, (2) saturation, and (3) annihilation.

The first threshold is the coherent control limit, which is the most difficult to establish since different control mechanisms have been proposed involving a different number of interactions with the laser field and thus exhibiting different intensity

dependences. For example, Brumer and co-workers^{2,38,39} formulated a one-photon (two matter–field interactions) control mechanism to coherently manipulate reactions ($k = 1, n = 2$). However, most experimental coherent control studies invoke mechanisms that require additional matter–field interactions such as the manipulation of coherent electronic states (odd n)⁴ or the formation and manipulation of vibrational wave packets.^{4,9,40} The launching of wave packets requires two matter–field interactions, e.g., one photon for excited-state wave packets and no (net) photons for ground-state wave packets ($k = 1, n = 2$),³⁶ and subsequent matter–field interactions with these wave packets will increase n . Since the focus of this manuscript is to characterize incoherent effects (e.g., saturation and annihilation) that make the characterization of optimal control mechanisms difficult, we concentrate on simulating only these processes.

The next two intensity thresholds, in contrast to the optimal control mechanism above, are of incoherent origin but may contribute to optimal control experiments. The first of those is the saturation limit that is reached when the probability of multiple matter–field interactions occurring on the *same* molecule becomes appreciable.⁴¹ Assuming these interactions occur within the lifetime of the initially excited state, saturation then results from the excitation of the ground state and de-excitation (via SE) of the same chromophore ($k = 1, n = 4$). This requires two matter–field interactions to excite and then two more interactions to de-excite the same chromophore.

The intensity threshold for annihilation occurs only in systems consisting of *coupled* chromophores (e.g., LH2) and is reached when the probability of exciting more than one molecule on the complex is nonnegligible. For optical excitation of the LH2 complexes of *Rps. acidophila* ($k = 9, n = 4$), this results from exciting multiple carotenoid molecules within a single LH2 ring, which will in turn produce multiple excited B850 chromophores after EET. These multiple excitations will then migrate within the LH2 ring until they interact on the same B850 chromophore, leading to singlet–singlet annihilation and the net loss of excitations.^{33,35,42} As the number of interacting chromophores increases (and assuming full excitation mobility), then annihilation contributions to the collected signals will be enhanced since the probability of exciting multiple chromophores on the same complex will become higher. As a result, weak excitation intensities are required to observe annihilation-free signals in large systems.^{33,43}

Annihilation differs from saturation because it is realized when multiple interactions occur on the *same LH2 ring*, whereas saturation occurs when multiple photon interactions occur on the *same chromophore*. Obviously the onset of saturation is at excitation intensities higher than annihilation, and for LH2 this will be at approximately 9 times greater intensity since each LH2 ring contains nine carotenoids (more so for aggregated LH2 systems). The multistate models discussed in paper 1 and modified to account for annihilation incorporate both saturation and annihilation at the appropriate intensity thresholds. It must be clearly noted that in coherent control experiments the observed dynamics attributed to coherent control mechanisms must coexist and compete with saturation effects. Furthermore, if the studied sample consists of multiple coupled chromophores, then annihilation effects *will* also contribute to the dynamics and hence interfere with the determination of any coherent control mechanisms in the experiment.

5.2. Saturation versus Annihilation. The multistate models described in paper 1, when extended with the annihilation approach described in section 4, exhibit all the salient features of the pump–probe signals from the LH2 samples including:

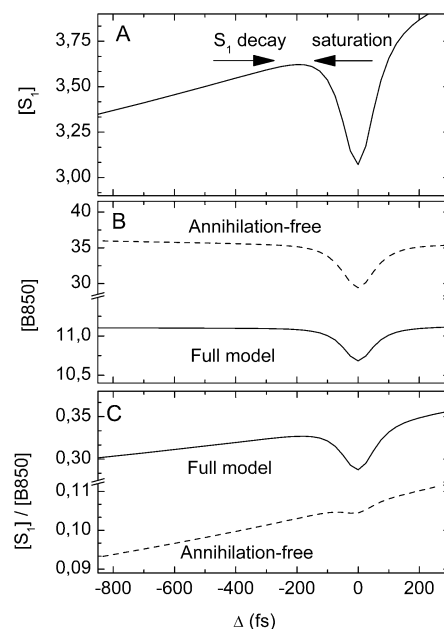


Figure 8. Simulated action traces PPP signals at a 4-ps probe time for S_1 and a 10-ps probe time for B850 populations. (A) $[S_1]$ PPP signal dynamics and (B) $[B850]$ signal dynamics with different levels of annihilation: annihilation-free (dashed curve) and full annihilation (solid curve). (C) The $[S_1]/[B850]$ population ratio for the two annihilation limits in part B. Model parameters are in the caption of Figure 5.

- EET dynamics from rhodopin glucoside to the B850 bacteriochlorophylls,
- saturation phenomena from overpumping S_2 ,
- dynamics of both the relevant carotenoid populations (S_1 , S^* , and S_2 , triplet) and the B850 population,
- interchromophore annihilation dynamics within the B850 manifold,
- excitation-intensity-dependent S^* , S_1 , and B850 populations, and
- intersystem crossing on B850 and subsequent quenching of the BChl triplets by the carotenoids.

A comparison of the simulated (Figure 7) and experimental action trace data (Figure 4) demonstrates that these models capture the qualitative nature and many of the quantitative properties of the measured intensity- and time-dependent multipump signals. Consequently, the modeling outlined here and in paper 1 is particularly useful for interpreting the optimal control results of Herek and co-workers^{18,23} and can be easily extended to the interpretation of other optimal control experiments.

The utility of the PPP action trace signals to aid in interpreting excitation pulse sub-structure from the optimal control experiment¹⁸ is highlighted in Figure 8, where the simulated PPP action traces of the S_1 and B850 states with differing levels of annihilation are contrasted. If the target goal in the LH2 control experiment were to optimize solely the S_1 excited-state population by varying only the excitation pulse separations, then the obtained optimal pulse separation would be ~ 200 fs (at this set of excitation intensities). This optimized separation results from competition between two opposing factors: (1) *increasing* the pulse separation to reduce the effects of saturation and (2) *reducing* the pulse separation to maximize the S_1 populations before they decay back to the ground state.

The $[S_1]/[B850]_{\text{tot}}$ ratio (constructed to represent the IC/EET branching from rhodopin glucoside¹⁸) consist of signals that exhibit qualitatively, but not quantitatively, similar saturation properties since both originate from the same excitation event.

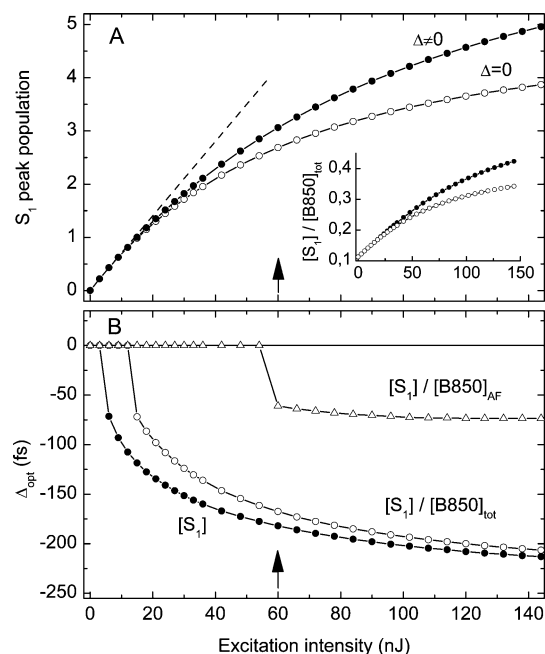


Figure 9. Simulated power dependence. (A) Maximum in S_1 population at 4 ps, when both pump pulses are temporally overlapped, $\Delta = 0$ (open circles), and optimized for maximum population ($\Delta \neq 0$) as a function of Δ (filled circles). The dashed line indicates the “linear regime” commonly assumed for a saturation-free experiment. (B) The predicted pulse separation, Δ_{opt} , resulting from optimizing the $[S_1]/[B850]_{\text{tot}}$ ratio (filled circles) and $[S_1]/[B850]_{\text{AF}}$ (open circles). For contrast, the pulse separation obtained when optimizing only $[S_1]$ is shown (open triangles). The arrows show the pulse intensity for the model calculations shown in Figures 5–9, and the model parameters are in the caption of Figure 6.

This results in a ratio that reduces, but not completely cancels, the saturation phenomena from the optimization. In contrast, if both signals were conservative (i.e., not independently modulated by other intensity-dependent mechanisms such as annihilation), then the saturation effects would fully cancel. The optimization of such signals involving only incoherent effects would maximize at $\Delta = 0$ and allow for the clear study of interesting optimal control mechanisms. It should be noted that even in the absence of annihilation a weak dip does result (Figure 8C, dashed line) from the multiple, intensity-dependent, EET pathways in the underlying two-photon model.

Introduction of annihilation into the model enhances the saturation effects into the optimization (Figure 8C, solid line), and the optimization of the $[S_1]/[B850]_{\text{tot}}$ ratio will then preferentially amplify the S_1 population. Though saturation effects must contribute to most optimal control experiments (except those that involve one-photon mechanisms), optimizing the ratio of conservative signals will not necessarily remove such interfering contributions. This is of particular importance for the optimal control studies of multichromophore systems where nonconservative signals are expected (e.g., light-harvesting proteins,^{33,42} molecular crystals,⁴⁴ and conjugated polymers^{44,45}).

The characterization and separation of true coherent mechanisms from trivial incoherent effects such as saturation and annihilation may be partially accomplished with an excitation intensity dependence study of the optimization properties. Figure 9A contrasts the simulated excitation pulse intensity dependence for $[S_1]$ when the $[S_1]/[B850]_{\text{tot}}$ ratio is optimized ($\Delta \neq 0$) or not ($\Delta = 0$). Both curves initially increase linearly with increasing pulse intensity but deviate with characteristic saturation behaviors,^{41,46} although at different thresholds. When Δ is

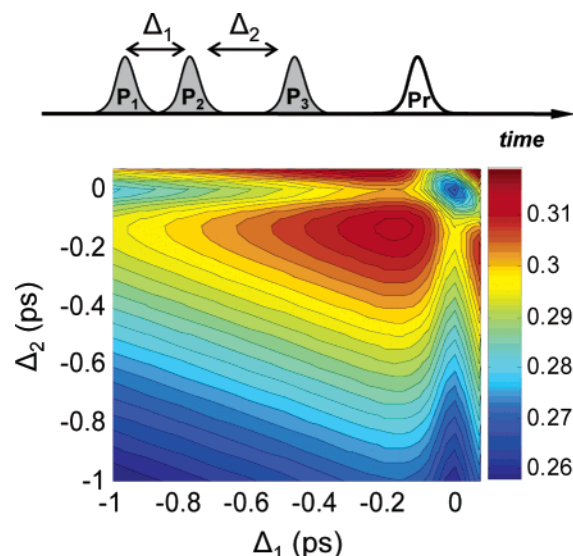


Figure 10. Simulated three-pulse pump action signal, with the probe time at 4 ps. The maximum is at $\Delta_1 = 200$ fs and $\Delta_2 = 180$ fs. The sum of pulse intensities is the same as that in the two-pulse experiment (120 nJ), with equal pulse energies. Model parameters are in the caption of Figure 6.

increased, the optimized S_1 population signal is made more “linearized” with an increase in signal amplitude resulting from reduced saturation. Inspection of the $[S_1]/[B850]_{\text{tot}}$ ratio (inset) shows that the threshold for deviating from the linear regime is increased to ~ 40 nJ, due to the incomplete canceling of saturation effects in the $[S_1]/[B850]_{\text{tot}}$ ratio.

The corresponding pulse separations obtained from optimizing $[S_1]/[B850]_{\text{tot}}$ (open circles) and only $[S_1]$ (filled circles) are contrasted in Figure 9B. As expected, the optimal pulse separations, Δ_{opt} , for both signals increase at higher pulse intensities because of the increased contribution of saturation to the signals. Although the optimized PPP intensities increase continuously with increasing pulse intensities (Figure 9A), the resulting Δ_{opt} values do not evolve nearly so smoothly; the sudden jumps from $\Delta = 0$ to a nonzero values results from the peculiar properties of the PPP action traces and is discussed in detail in the Supporting Information. The Δ_{opt} values for $[S_1]$ are greater than those for $[S_1]/[B850]_{\text{tot}}$, which are much greater than the annihilation-free ratio, $[S_1]/[B850]_{\text{AF}}$ (open triangles). For the $[S_1]/[B850]_{\text{AF}}$ ratio, the nonzero Δ_{opt} values observed at high intensities arise from the intrinsic improper cancellation of saturation due to the intensity-dependent S_1/S^* branching in the two-photon model (which is also observed in the inhomogeneous model). Although the PPP signals and thus control experiments can be measured in the “saturation-free” intensity regime, the combination of the small differences between the optimized and the unoptimized signals and the high sensitivity of the experiment will result in discernible pulse separations in the optimized experiment.

5.3. Three-Pump Signals. To more closely predict optimal control experiments where often many subpulses are observed, additional pump pulses were introduced into the numerical simulations. In Figure 10, the two-dimensional action signals for the $[S_1]/[B850]_{\text{tot}}$ ratio are shown for a simulated three-pump experiment as function of the two-pulse separations: Δ_1 and Δ_2 . A maximum in the S_1 population is observed when the excitation pulses are separated by ~ 180 and ~ 200 fs. This asymmetry in the simulated signal results from the pump-induced depletion effects that differ because the depletion is sensitive to whether a strong pump pulse (i.e., two temporally

overlapped pump pulses) interacts with the sample before a second weaker pump pulse or vice versa. The multipump simulations presented in this manuscript use pulses of equal intensities; however, if allowed to vary, the optimization of the pump intensities will shift the maximum to a more symmetric position. Moreover, the optimal intensity pattern (e.g., 30, 60, and 30 nJ for the P_1 , P_2 , and P_3 pump pulses, respectively) is similar to the intensities observed in the Herek et al. study,^{18,23} suggesting that in addition to pulse separations this degree of freedom is also optimized in their optimal control experiment, as expected.

Although the experimental and simulated results for the two- and three-pulse signals strongly suggest that the pulse separations (and intensities) observed in optimal control studies result from an interplay of interfering incoherent mechanisms, a full quantified explanation of the 250-fs pulse separations identified in the Herek et al. control study^{18,23} was not successful (only ~200 fs from Figure 10) with the simulations presented here. Clearly, more complete numerical simulations involving sequences of 8–10 excitation pulses with variable pulse separations and intensities are required. Such calculations are beyond the scope of this manuscript and are left for further exploration. It must be further noted that this modeling does not address the nature of the optical phase relationship observed in the LH2 optimal control study,^{18,23} which may also contribute to the observed pulse separations.

6. Concluding Comments

Often in optimal control measurements, the applied laser pulse(s) must be of sufficient intensities to ensure multiple matter–field interactions with a particular chromophore, implying that underlying coherent control mechanisms must coexist and thus compete with saturation effects. Moreover, if the investigated sample is multichromophoric, then annihilation effects will also contribute to the experiment. Saturation, unlike coherent control mechanisms, is an incoherent and trivial optimization phenomenon that also shapes excitation pulse profiles and can be removed by optimizing a ratio of *conservative* population signals (e.g., not modulated by external post-excitation factors such as annihilation) instead of only a population signal. However, if a ratio of nonconservative signals is optimized, then the incomplete cancellation of saturation effects will reintroduce this interfering mechanism into the optimization procedure and potentially obscure the results.

In the LH2 coherent control experiment by Herek et al.,¹⁸ the observed multipulse excitation profile was obtained from optimizing the ratio of energy flow from S_2 to S_1 by IC and from S_2 to B850 by EET. At the excitation intensities necessary for performing the experiment, the B850 signal is nonconservative since it is strongly affected by singlet–singlet annihilation. Thus, optimizing the IC/EET ratio incompletely removes the saturation contributions to the experiment. The multistate models proposed in paper 1 predict an optimal pulse separation between two pump pulses that maximizes the $[S_1]/[B850]_{\text{tot}}$ ratio, which is in near-quantitative agreement with the results of the coherent control experiment.¹⁸ This separation results exclusively from incoherent contributions, i.e., the interplay between saturation effects (*increasing* the separation of the excitation pulses) and the lifetime of S_1 (*reducing* pulse separation).

Although our simulations and experiments do not address the phase dependence observed in the original Herek et al.¹⁸ measurement for LH2, our model captures the main structural features and emphasizes the importance of separating incoherent population effects from pulse shaping experiments to access new

information on the relationships of time-dependent wave functions. It should be noted that saturation effects are not limited to optimal control studies on the LH2 system and other samples with rapidly changing transition dipole moments should exhibit similar contributions. For example, the rapid shifting of the fluorescence band from polar solvation dynamics⁴⁷ or fast excited-state reactions such as proton transfer⁴⁸ and isomerization^{49,50} should produce similar effects; recently multipulse saturation curves have been observed in single-molecule experiments involving nonpolar chromophores in a rigid polymer glass.⁵¹ Unmistakably, incoherent saturation effects must be carefully accounted for when interpreting complex optimal control results on any sample.

Acknowledgment. We thank Professor Neil Hunter (University of Sheffield) for generously providing the *Rb. sphaeroides* LH2 samples that were initially used in these experiments. We are thankful to Professor Dwayne Miller (University of Toronto), Dr. Dorte Madsen (University of Southern California), Dr. Gert van der Zwan (Free University, Amsterdam), and Dr. Ben Brüggemann (Lund University) for constructive conversations and are also grateful to Professor Marcus Motzkus (University of Marburg) and Dr. Jennifer Herek (AMOLF, The Netherlands) for the sharing of unpublished data. This research was supported by The Netherlands Organization for Scientific Research via the division for Earth and Life Sciences. D.S.L. is grateful to the Human Frontier Science Program Organization for providing financial support with both long-term and short-term fellowships. L.V. was supported by a visitors grant from The Netherlands Organization for Scientific Research.

Supporting Information Available: Multipump signals from the LH2 complex isolated from *Rb. sphaeroides*, annihilation parameters, turnovers in action simulated traces, and potential mechanisms. This material is available free of charge via the Internet at <http://pubs.acs.org>.

Note Added in Proof: Brumer and co-workers have recently simulated results to explore new adaptive feedback experiments (Vogt et al. *Phys. Rev. Lett.* **2005**, *94*, 068305) and found no coherent types of control. The only control that they do observe is essentially incoherent (*Phys. Rev. Lett.* **2005**, *95*, 168306), which supports this paper's emphasis on the importance of identifying and characterizing incoherent contributions in optimal control experiments.

References and Notes

- (1) Assion, A.; Baumert, T.; Bergt, M.; Brixner, T.; Kiefer, B.; Seyfried, V.; Strehle, M.; Gerber, G. *Science* **1998**, *282*, 919.
- (2) Brumer, P.; Shapiro, M. *Sci. Am.* **1995**, *272*, 56.
- (3) Rice, S. A. *Science* **1992**, *258*, 412.
- (4) Rice, S. A.; Zhao, M. *Optical Control of Molecular Dynamics*; Wiley-Interscience: New York, 2000.
- (5) Kennis, J. T. M.; Larsen, D. S.; van Stokkum, I. H. M.; Vengris, M.; van Thor, J. J.; van Grondelle, R. *Proc. Natl. Acad. Sci. U.S.A.* **2004**, *52*, 17988.
- (6) Bardeen, C. J.; Yakovlev, V. V.; Wilson, K. R.; Carpenter, S. D.; Weber, P. M.; Warren, W. S. *Chem. Phys. Lett.* **1997**, *280*, 151.
- (7) Prokhorenko, V. I.; Nagy, A. M.; Miller, R. J. D. *J. Chem. Phys.* **2005**, *122*, 184502.
- (8) Daniel, C.; Full, J.; González, L.; Lupulescu, C.; Manz, J.; Merli, A.; Vajda, S.; Wöste, L. *Science* **2003**, *299*, 536.
- (9) Daniel, C.; Full, J.; Gonzalez, L.; Kaposta, C.; Krenz, M.; Lupulescu, C.; Manz, J.; Minemoto, S.; Oppel, M.; Rosendo-Francisco, P.; Vajda, S.; Wöste, L. *Chem. Phys.* **2001**, *267*, 247.
- (10) Weinacht, T. C.; White, J. L.; Bucksbaum, P. H. *J. Phys. Chem. A* **1999**, *103*, 10166.
- (11) Yip, F. L.; Mazziotti, D. A.; Rabitz, H. *J. Phys. Chem. A* **2003**, *107*, 7264.

- (12) Zhu, W. S.; Rabitz, H. *J. Chem. Phys.* **2003**, *119*, 3619.
- (13) Zhu, W. S.; Rabitz, H. *J. Chem. Phys.* **1999**, *111*, 472.
- (14) Zhu, W. S.; Botina, J.; Rabitz, H. *J. Chem. Phys.* **1998**, *108*, 1953.
- (15) Weiner, A. M. *Rev. Sci. Instrum.* **2000**, *71*, 1929.
- (16) Verluise, F.; Laude, V.; Cheng, Z.; Spielmann, C.; Tournois, P. *Opt. Lett.* **2000**, *25*, 575.
- (17) Meshulach, D.; Yelin, D.; Silberberg, Y. *J. Opt. Soc. Am. B* **1998**, *15*, 1615.
- (18) Herek, J. L.; Wohlleben, W.; Cogdell, R. J.; Zeidler, D.; Motzkus, M. *Nature* **2002**, *417*, 533.
- (19) Meshulach, D.; Silberberg, Y. *Nature* **1998**, *396*, 239.
- (20) Wohlleben, W.; Buckup, T.; Herek, J. L.; Cogdell, R. J.; Motzkus, M. *Biophys. J.* **2003**, *85*, 442.
- (21) Rondonuwu, F. S.; Yokoyama, K.; Fujii, R.; Koyama, Y.; Cogdell, R. J.; Watanabe, Y. *Chem. Phys. Lett.* **2004**, *390*, 314.
- (22) Macpherson, A. N.; Arellano, J. B.; Fraser, N. J.; Cogdell, R. J.; Gillbro, T. *Biophys. J.* **2001**, *80*, 923.
- (23) Wohlleben, W.; Buckup, T.; Herek, J. L.; Motzkus, M. *ChemPhysChem* **2005**, *6*, 850.
- (24) Papagiannakis, E.; van Stokkum, I. H. M.; Vengris, M.; Cogdell, R. J.; van Grondelle, R.; Larsen, D. S. *J. Phys. Chem. B* **2005**, *110*, 5727.
- (25) Larsen, D. S.; van Stokkum, I. H. M.; Vengris, M.; van der Horst, M.; de Weerd, F. L.; Hellingwerf, K.; van Grondelle, R. *Biophys. J.* **2004**, *87*, 1858.
- (26) Papagiannakis, E.; Larsen, D. S.; van Stokkum, I. H. M.; Vengris, M.; Hiller, R. G.; van Grondelle, R. *Biochemistry* **2004**, *43*, 15303.
- (27) Larsen, D. S.; Papagiannakis, E.; van Stokkum, I. H. M.; Vengris, M.; Kennis, J. T. M.; van Grondelle, R. *Chem. Phys. Lett.* **2003**, *381*, 733.
- (28) Larsen, D. S.; Papagiannakis, E.; van Stokkum, I. H. M.; Vengris, M.; Kennis, J. T. M.; van Grondelle, R. *Chem. Phys. Lett.* **2003**, *381*, 733.
- (29) Wohlleben, W.; Buckup, T.; Hashimoto, H.; Cogdell, R. J.; Herek, J. L.; Motzkus, M. *J. Phys. Chem. B* **2004**, *108*, 3320.
- (30) Sundström, V.; Pullerits, T.; van Grondelle, R. *J. Phys. Chem. B* **1999**, *103*, 2327.
- (31) Rondonuwu, F. S.; Watanabe, Y.; Zhang, J. P.; Furuichi, K.; Koyama, Y. *Chem. Phys. Lett.* **2002**, *357*, 376.
- (32) Trinkunas, G.; Herek, J. L.; Polivka, T.; Sundström, V.; Pullerits, T. *Phys. Rev. Lett.* **2001**, *86*, 4167.
- (33) van Amerongen, H.; Valkunas, L.; van Grondelle, R. *Photosynthetic Excitons*; World Scientific: Singapore, 2000.
- (34) van Grondelle, R. *Biochim. Biophys. Acta* **1985**, *811*, 147.
- (35) Brüggemann, B.; Herek, J. L.; Sundström, V.; Pullerits, T.; May, V. *J. Phys. Chem. B* **2001**, *105*, 11391.
- (36) Mukamel, S. *Principles of Nonlinear Optical Spectroscopy*; Oxford University Press: New York, 1995.
- (37) Valkunas, L.; van Grondelle, R.; Larsen, D. S., manuscript in preparation.
- (38) Batista, V. S.; Brumer, P. *J. Chem. Phys.* **2001**, *114*, 10321.
- (39) Brumer, P.; Shapiro, M. *Chem. Phys.* **1989**, *139*, 221.
- (40) Hornung, T.; Meier, R.; Motzkus, M. *Chem. Phys. Lett.* **2000**, *326*, 445.
- (41) Demtröder, W. *Laser Spectroscopy*, 2nd ed.; Pergamon Press: New York, 1987.
- (42) Valkunas, L.; Trinkunas, G.; Liuolia, V.; van Grondelle, R. *Biophys. J.* **1995**, *69*, 1117.
- (43) Papagiannakis, E.; Kennis, J. T. M.; van Stokkum, I. H. M.; Cogdell, R. J.; van Grondelle, R. *Proc. Natl. Acad. Sci. U.S.A.* **2002**, *99*, 6017.
- (44) Pope, M.; Swanberg, C. E. *Electronic Processes in Organic Crystals and Polymers*; Oxford University Press: New York, 1999.
- (45) Gadermaier, C.; Cerullo, G.; Sansone, G.; Leising, G.; Scherf, U.; Lanzani, G. *Phys. Rev. Lett.* **2002**, *89*, 117402.
- (46) Groot, M. L.; van Grondelle, R.; Leegwater, J. A.; van Mourik, F. *J. Phys. Chem. B* **1997**, *101*, 7869.
- (47) Castner, E. W.; Maroncelli, M.; Fleming, G. R. *J. Chem. Phys.* **1987**, *86*, 1090.
- (48) Mandal, D.; Tahara, T.; Meech, S. R. *J. Phys. Chem. B* **2004**, *108*, 1102.
- (49) Vengris, M.; van der Horst, M.; Zgrablic, G.; van Stokkum, I. H. M.; Haacke, S.; Chergui, M.; Hellingwerf, K. J.; van Grondelle, R.; Larsen, D. S. *Biophys. J.* **2004**, *87*, 1848.
- (50) Hasson, K. C.; Gai, F.; Anfinrud, P. A. *Proc. Natl. Acad. Sci. U.S.A.* **1996**, *93*, 15124.
- (51) van Dijk, E. M. H. P.; Hernando, J.; Garcia-Lopez, J.-J.; Crego-Calama, M.; Reinhoudt, D. N.; Kuipers, L.; Garcia-Parajo, M. F.; van Hulst, N. F. *Phys. Rev. Lett.* **2005**, *94*, 078302.